# Unraveling the link between magma and deformation during slow seafloor spreading

Yanghui Zhao[1], Weiwei Ding[2], Gianreto Manatschal[3], Xiaodong Wei[1], Hanghang Ding[4], Zhengyi Tong[5], and Jingyan Zhao[1]

[1]Second Institute of Oceanography, Ministry of Natural Resources
[2]the Second Insitiue of Oceanography, State Oceanic Administration of China
[3]EOST-UDS, Strasbourg
[4]The Second Institute of Oceanography, Ministry of Natural Resources, China
[5]School of Earth Sciences, Zhejiang University

October 27, 2023

## Abstract

Detachment faulting related to oceanic core complexes (OCCs) has been suggested to be a manifestation of slow seafloor spreading. Although numerical models suggest OCCs form under low magma supply, the specific interaction between magmatism and tectonic faulting remains elusive. This paper examines seismic observations detailing the spatiotemporal interactions between magmatism, high-angle faulting, and detachment faulting at a slow-spreading mid-ocean ridge in the West Philippine Basin. We identified a magma-rich spreading phase at 36 Ma, indicated by a magmatic top basement and normal oceanic crust with shallow-penetrating high-angle faults. An axial valley reveals an along-strike transition from normal to highly tectonized oceanic crust over a distance of 70 km. Two older OCCs with concave-down fault geometries and a younger OCC with steep-dipping faulting suggest sequential detachments with the same polarity. Our findings suggest: (1) slow seafloor spreading is cyclical, alternating between high-angle faulting with a relatively high magma supply and detachment faulting with limited magma supply; (2) sequential development of younger detachments in the footwall of its predecessor leads to an asymmetric split in the newly accreted crust; and (3) the life cycle of OCC ends with high-angle faults that overprint the detachment and act as magma pathways, sealing the OCC. Our study captures the dynamic interaction between high-angle and detachment faults and their concurrent and subsequent relationship to magmatic systems. This reveals that strain distribution along strike is critical to OCC formation, thus enriching our understanding beyond conventional considerations such as spreading rates and melt budgets at mid-ocean ridges.

## Hosted file

976394_0_art_file_11473578_s2g3qc.docx available at https://authorea.com/users/673210/articles/672089-unraveling-the-link-between-magma-and-deformation-during-slow-seafloor-spreading

Unraveling the link between magma and deformation during slow seafloor spreading

Yanghui Zhao[*a], Weiwei Ding[**a,b], Gianreto Manatschal[c], Xiaodong Wei[a], Hanghang Ding[d], Zhengyi Tong[d], Jingyan Zhao[a]

[a]Key Laboratory of Submarine Geosciences, Second Institute of Oceanography, Ministry of Natural Resources, Hangzhou 310012, China

[b]School of Oceanography, Shanghai Jiao Tong University, Shanghai, 200030, China

[c]Université de Strasbourg, CNRS, ITES UMR 7063, Strasbourg F-67084, France;

[d]School of Earth Sciences, Zhejiang University, Hangzhou 310027, China

E-mail addresses: zhaoyh@sio.org.cn (Y. Zhao), wwding@sio.org.cn (W. Ding).

## Abstract

Detachment faulting related to oceanic core complexes (OCCs) has been suggested to be a manifestation of slow seafloor spreading. Although numerical models suggest OCCs form under low magma supply, the specific interaction between magmatism and tectonic faulting remains elusive. This paper examines seismic observations detailing the spatiotemporal interactions between magmatism, high-angle faulting, and detachment faulting at a slow-spreading mid-ocean ridge in the West Philippine Basin. We identified a magma-rich spreading phase at 36 Ma, indicated by a magmatic top basement and normal oceanic crust with shallow-penetrating high-angle faults. An axial valley reveals an along-strike transition from normal to highly tectonized oceanic crust over a distance of 70 km. Two older OCCs with concave-down fault geometries and a younger OCC with steep-dipping faulting suggest sequential detachments with the same polarity. Our findings suggest: (1) slow seafloor spreading is cyclical, alternating between high-angle faulting with a relatively high magma supply and detachment faulting with limited magma supply; (2) sequential development of younger detachments in the footwall of its predecessor leads to an asymmetric split in the newly accreted crust; and (3) the life cycle of OCC ends with high-angle faults that overprint the detachment and act as magma pathways, sealing the OCC. Our study captures the dynamic interaction between high-angle and detachment faults and their concurrent and subsequent relationship to magmatic systems. This reveals that strain distribution along strike is critical to OCC formation, thus enriching our understanding beyond conventional considerations such as spreading rates and melt budgets at mid-ocean ridges.

Keywords: slow mid-ocean ridges; life cycle of oceanic core complex; fault pattern variation; tectonic-magmatism interaction.

# 1. Introduction

The spreading rate is often considered a key factor in controlling crustal accretion at mid-ocean ridges (MORs) (e.g., Bell and Buck, 1992; Chen and Morgan, 1990). Oceanic core complexes (OCCs) at slow spreading rates of ~14-32mm/yr on the Mid-Atlantic Ridge (MAR, e.g., Cann et al., 1997; Zhang et al., 2022a) and the Southwest Indian Ridge (SWIR, e.g., Cannat et al., 2006) with rates less than 14 mm/yr, have led to the idea that long-lived detachment faults split plates as the proportion of tectonic extension increases in areas with a low melt supply (e.g., Lin et al., 1990; Tucholke et al., 2008). This idea is further supported by numerical models, suggesting that magma controls the initiation and termination of detachment faulting. Specifically, as magma supply diminishes below a certain threshold, it can trigger the formation of large-offset detachment faults, leading to the exhumation of the oceanic lower crust (gabbros) and mantle on the seafloor (Buck et al., 2005; Huismans and Beaumont, 2003; Lavier et al., 1999).

Several kinematic models of oceanic crust accretion at slow and ultraslow MORs have been proposed (**Fig. 1**). At the slow MAR, a long-lived detachment model (OCC/corrugated surfaces) has been suggested (MacLeod et al., 2009). This model posits an OCC initiation with a detachment fault developing through runaway weakening of a high-angle normal fault, subsequently being cut by dikes, and eventually terminates when sufficient melt is delivered to the detachment footwall (**Figs. 1A-1C**). Subsequently, a dynamic model for successive, short-lived detachment faults has been proposed by Reston and McDermott (2011) (**Figs. 1D-1F**). This model has been applied to the ultraslow spreading SWIR, where detachment faulting with flipping polarity controls mantle exhumation and terminates when extrusion occurs in a magma-starved context (c.f. “flip-flop” model, Sauter et al., 2013). The comparison of these models highlights that the type of fault pattern closely relates to the melt supply. Long-lived detachments occur with a moderate melt supply, whereas short-lived flip-flop detachment faults arise when the melt supply is low.

However, field observations from the Alpine Tethys do not fit the above models; in particular, magmatism may persist during active detachment faulting (MacLeod et al., 2002; Manatschal et al., 2011; Coltat et al. 2020). In addition, various petrological and numerical studies suggest the role of magma supply in detachment fault development and its contribution to strain localization at the root of these faults during slow seafloor spreading (Behn and Ito, 2008; Cannat et al., 1991; Hansen et al., 2013; Howell et al., 2019; Olive et al., 2010; Schroeder and John, 2004; Tian and Choi, 2017). Although these studies provide indirect evidence of magmatism facilitating detachment fault formation, direct observations on how magma supply triggers such faults and interacts with crust accretion during faulting are limited. Moreover, the interaction between magmatic and fault activity is crucial to control and/or modify the thermal state and the rheology of divergent plate boundaries at MORs (Cannat et al., 2019). Unraveling the link between magma and deformation, and indirectly, the rheology is feasible through high-quality seismic reflection sections.

Here, we present new observations from multichannel seismic (MCS) reflection profiles A-A' and B-B' that allow imaging the detailed crustal structures of a slow-spreading MOR in the eastern West Philippine Basin (WPB) (**Fig. 2**). The MOR of the WPB, also known as the Central Basin Fault (CBF, e.g., Deschamps et al., 2002), experienced significant spreading reorientation in its eastern part, transitioned from NW-SE to E-W, accompanied by dramatic topographic changes from a gentle side valley to a steep, narrow valley (**Figs. 2B**). Profile A-A' is situated within this eastern part of the CBF, starting at the southwest ridge flank and ending at the northern shoulder, extending 130 km oblique to the CBF. Profile B-B' extends from NW-SE, situated at the eastern extremity of the N-S spreading valley. The 30° angle at which the MCS profile A-A' intersects the spreading axis facilitates a simultaneous observation of oceanic crustal structures measuring 65 km across ridge and 112 km along strike, and profile B-B' across ridge provides further validation of the structures at the eastern end of the CBF. Thus, these profiles allow us to assess both the spatial changes in the oceanic crustal structure at comparable spreading rates and the interaction between magmatism and tectonic faulting during the slow spreading process at the MOR.

## 2. Geological Setting

The eastern MOR of the WPB exemplifies a typical slow-spreading MOR system, characterized by a deep axial valley bounded by ridge shoulders with a 500-m relief (**Fig. 2**). Water depth in the WPB ranges between 3-6 km, with the seafloor generally shallowing from west to east (Deschamps et al., 2002). Predominantly, sediments of the WPB comprise abyssal deposits with thicknesses under 300 m (Zhang et al., 2022b). Pronounced segmentation of the axial valley suggests that the seafloor spreading in the

WPB has undergone multiple episodes of reorientations (Deschamps et al., 2002). The specific area of our study is situated between 132° E and 133.5° E longitude and 14.5° N and 147° N latitude, where a reorientation of seafloor spreading from N-S to NE-SW occurred.

### 2.1 N-S slow seafloor spreading during 45-33 Ma

The initial seafloor spreading of the WPB is estimated to have occurred around 60 Ma (Hilde and Lee, 1984), 55 Ma (Deschamps and Lallemand, 2002; Hall, 2012), 52-51 Ma (Ishizuka et al., 2013), or 50 Ma (Arculus et al., 2019). Before 45 Ma, the seafloor spreading direction was N10W at a moderate spreading rate (half-rate of 44 mm/a) (**Fig. 3A**). Around 45 Ma, significant plate reorganization occurred from Southeast Asia through the western Pacific to Australia, including a notable slowdown of the subduction of marginal basins along the Philippine Arc (Ding et al., 2023; Hall, 2002) (**Figs. 3B and 3D**). Consequently, the driving force for seafloor spreading in the WPB weakened, leading to a reduction in the spreading half-rate to 18 mm/a.

### 2.2 NE-SW slow seafloor spreading post 33 Ma

Between approximately 33-30 Ma, a regional extension likely prompted the most recent reorientation of spreading from N-S to NE-SW (**Figs 3C - 3D**). This reorientation is substantiated by the NW-SE-directed spreading fabrics that intersect the E-W fabrics (Deschamps et al., 2002). Although the precise timing of this last reorientation is uncertain, the occurrence of this spreading is hypothesized to fall within the period of

33-26 Ma if we assume the basalts from the ridge walls were formed during the NW-SE oriented spreading (Fujioka et al., 1999; Ishizuka et al., 2011).

Following the cessation of seafloor spreading in the WPB, the proto Kyushu-Palau Ridge (KPR) was divided into the current KPR and the Izu-Bonin-Mariana (IBM) arcs (Ishizuka et al., 2011). This division might be prompted by the rollback of the subducting Pacific plate, which in turn stimulated the back-arc spreading in the Shikoku-Parece Vela basin and triggered an eastward tectonic-magmatic migration (Okino et al., 1998).

# 3. Data and Method

The seismic reflection profiles A-A' and B-B' were acquired in 2020 by the R/V “Dayanghao”, Second Institute of Oceanology, Ministry of Natural Resources, China. The seismic reflection source was an air gun array with a total volume of 6040 cubic inches, which was fired at regular 37.5 m intervals with a vessel speed of ~5 knots. Seismic signals were recorded with a 6-km-long streamer (480-channel). The record length was 14 s with a sampling rate of 2 ms. Data were processed and conditioned through several iterations of processing and imaging flows to produce the final time-migrated and depth-migrated sections. The Root Mean Square velocities used in time migration processing are converted to interval velocities using the Dix formula (Dix, 1955). The relative variations in the interval velocities are related to the density variations along the profiles.

Bathymetric data (https://topex.ucsd.edu/WWW_html/srtm15_plus.html), free-air gravity anomaly (https://topex.ucsd.edu/pub/global_grav_1min/), and magnetic anomaly (https://www.ngdc.noaa.gov/geomag/emag2.html) are individually extracted from global grids. Bouguer gravity anomalies are computed from free-air gravity anomalies and topography grids.

## 4. Seismic Observation and Interpretation

The main seismic profile A-A' crosses three bathymetric highs: the southern ridge shoulder, the structural high within the spreading valley, and the northern ridge shoulder (**Fig. 2B**). Both southern and northern ridge shoulders exhibit high free-air gravity anomalies, with the northern ridge shoulder showing much higher magmatic anomalies compared to the southern ridge shoulder (**Figs. 4A and 5A**). The structural high, situated between these two ridge shoulders, partitions the profile into N-S and NE-SW valleys (**Fig. 2B**), reflecting the latest spreading reorientation from N-S to NE-SW (**Fig. 3**).

Based on these observations, we divide the profile A-A' into three segments: Segment ① across the southwest ridge flank of the WPB; Segment ② across the latest NE-SW spreading axis, bounded by the southern ridge shoulder and structural high; Segment ③ across the N-S spreading axis and the northern ridge shoulder.

We present seismic reflection features from SW to NE, Segment by Segment. We first propose a classification of the observed reflectors, denoted by R1 – R20 in **Figs. 4-5**; then describe the reflection features and their interpretations, group by group (**Table 1**).

### 4.1 Segment ①: Southwest ridge flank

4.1.1 Top basement

The seafloor of Segment ① can be observed at a depth of 6-7 s TWTT (~5.2-5.5 km below sea level) with both smooth and jagged reflections (**Fig. 4**). Smooth seafloor can be observed at a distance of 12-22km along the profile (marked as Smoo1 in **Fig. 4B**), with a thin layer of parallel reflectors underneath (colored green in **Fig. 4C**). Jagged seafloor (marked as Jag1) is characterized by sub-horizontal reflectors interrupted by high-angle dipping reflectors (R1, **Fig. 4B**). The NE-dipping reflectors at a distance of 0-15 km (R1) and the SW-dipping reflectors at 15-25 km (R2) form a symmetric rift pattern (**Fig. 4B**). These high-angle dipping reflectors penetrate 1 s TWTT in-depth below the seafloor and offset slightly rotated, alternative strong and weak reflectors. This set of shallow reflectors has low interval P-wave velocities (< 2.5 km/s, **Fig. 4D**). We interpret the high-angle dipping reflectors, R1 and R2, as high-angle normal faults (**Table 1**). These normal faults offset the top basement, resulting in the jagged seafloor (Jag1, **Fig. 4B**).

4.1.2 Intra basement

Below the seafloor, the upper unit (between the seafloor and the dotted pink line, **Fig. 4C**) shows moderate amplitude and disruptive reflectors in the MCS profile. This unit is characterized by low velocities (< 4 km/s, **Fig. 4D**) and is frequently penetrated by high-angle normal faults, R1 and R2 (**Figs. 4B-4D**). Contrastingly, the lower unit (below the dotted pink line, **Fig. 4C**) is delineated by a series of low-amplitude reflectors (Figs. 4B-4C) with high velocities ranging between 4.5-7 km/s (Fig. 4D). High-angle normal faults terminate at the boundary between the upper and lower units (dotted pink line, Figs. 4C-4D). A set of sub-horizontal and discontinuous reflectors (R3) are observed at a depth of ~ 9.5 s TWTT (Figs. 4B-4C). Below R3, velocities increase to > 7 km/s (Fig. 4D).

Given the velocity structure and normal faults penetration depth, the intra basement of Segment ① can be separated into upper and lower units (Figs. 4C-4D). The upper unit with low velocities (< 4 km/s, Fig. 4D) represents the upper crust, corresponding to the extrusive igneous layer of the oceanic crust penetrated by normal faults. The lower unit with high velocities (4.5-7 km/s, Fig. 4D) is interpreted as the lower crust, corresponding to the intrusive igneous layer of the oceanic crust. The sub-horizontal reflectors (R3, Fig. 4B) at the base of the lower crust are interpreted as the Moho.

Overall, Segment ① shows consistent seismic reflection features and uniform thickness. The observed seismic structures suggest a sufficient magma supply during oceanic crust accretion, resulting in a magmatic top basement in Segment ①.

## 4.2 Segment ②: NE-SW spreading valley

### 4.2.1 Top basement

The free-air gravity anomaly and Bouguer gravity anomaly values decrease rapidly from Segment ① to Segment ②, separated by the southern shoulder (Fig. 4A). Segment ② has rougher seafloor topography compared to Segment ①. The water depth increases dramatically from 6 s to 8 s TWTT (from 4.5 km to 5.5 km) over a distance of < 15 km from the southern ridge shoulder to the axial valley (**Fig. 4E**). The seafloor at the southern ridge shoulder shows high-amplitude reflectors (**Fig. 4B**). The seafloor at the SW side of the southern shoulder (distance of 22-35 km) is constituted by continuous reflectors with a short distance of smooth seafloor (Smoo2, **Fig. 4B**). A thin sequence beneath Smoo2 shows alternating strong and weak reflectors (green sequence, **Fig. 4C**).

The NE side of the southern shoulder (distance of 35-45 km) is jagged (Jag2, **Fig. 4B**) and interrupted by a set of high-angle dipping reflectors (R4, **Fig. 4B**) that dip parallelly to the NE and penetrate 2 s in-depth. In the spreading valley, high-angle dipping reflectors (R5 and R6, **Fig. 4B**) also frequently interrupt the seafloor, dipping parallelly to the southwest and penetrating 0.5 s TWTT in-depth below the seafloor.

Between R4, R5, and R6 (distance of 35-60 km), three groups of low-amplitude reflectors can be observed beneath the seafloor. These are individually highlighted as yellow, orange, and pink sequences in **Fig. 4C**. Specifically, the yellow sequences incline towards the SW, the orange sequences dip to the NE, and the pink sequences maintain a horizontal orientation (**Fig. 4C**). These shallowest sequences thicken towards the nearby high-angle dipping reflectors and exhibit low-velocity characteristics (< 2.5 km/s, **Fig. 4D**).

Similar to Segment ①, the green sequences beneath the smooth seafloor (Smoo2 and Smoo3 in **Fig. 4C**) are interpreted as sediments (**Table 1**). The high-angle dipping reflectors R4, R5, and R6 are interpreted as high-angle normal faults that dip in parallel (**Table 1**). Among them, faults R4 dip to the NE, resulting in a jagged seafloor shallowing to the southern shoulder. The three shallowest sequences, characterized by low velocities and color-coded as yellow, orange, and pink (**Fig. 4C**), are interpreted as magmatic extrusives (**Table 1**). Note that R5 exhibits a slightly higher amplitude and a more compact arrangement compared to R6 (**Fig. 4B**). Such observations indicate that the combination of orange sequences with R5 and the pink sequence with R6 might have originated in distinct chronological periods (for detailed discussion, refer to Section 5.2).

#### 4.2.2 Intra basement of the NE-SW spreading valley

Below the top basement, three sets of SW-dipping reflectors, R7, R8, and R9, can be observed (**Fig. 4B**). Specifically, R7 displays moderately continuous patterns with medium amplitude and spans the entire length of the spreading valley at a depth of 7.5-9.5 s TWTT. High velocities (> 5.5 km/s) run alongside R7 from the deep (9.5 s TWTT) up to the shallow levels (7.5 s TWTT) (**Fig. 4D**). In the depth-migrated section after obliquity correction, the shallow part of R7 presents a gentle angle at the surface, with true dips less than 15° (**Fig. 4E**). In contrast, the deepest part of R7 becomes steep, exhibiting true dips of 62°, and offsets sub-horizontal reflectors, R3, at a depth of 9.5 s TWTT (**Fig. 4B**, 9.5 km in **Fig. 4E**). Overall, R7 forms a concaved-down geometry and is marked by a large-scale surface expression, encapsulating the high velocities within its bounds (**Figs. 4C - 4E**).

R8 is observed at a depth of 8-9.5 s TWTT and spans a distance of 45-50 km (**Fig. 4B**). The majority of R8 maintains a straightforward planar geometry and aligns parallelly to R7. Notably, R8 intersects with the sub-horizontal reflectors R3 at 9.5 s TWTT depth and merges with R7 closer to the surface (**Fig. 4C**). R8 does not show any notable features in its velocity structures (**Fig. 4D**).

Contrastingly, R9 stands out with a more pronounced amplitude and displays more consistent patterns than both R7 and R8 (**Fig. 4B**). R9 exhibits a steeply inclined posture and links up with laterally extending reflectors, R10, at more superficial depths. R10 consists of three sets of sub-horizontal reflectors, forming a constructive structure with a relief of 0.5 km above the seafloor within the spreading valley (**Figs. 2B and 4B**). The region encapsulated by R9 and R10 shows high velocities of > 5.5 km/s (**Fig. 4D**). At a depth of 9.5 s TWTT, R7, R8, and R9 terminate at sub-horizontal reflector R3, and an increase in velocity is observed beneath R3. Along both R7 and R9, high velocities are observed to span from beneath R3 (at depths exceeding 9.5 s TWTT) to more superficial levels.

While R7, R8, and R9 all exhibit a SW-dipping orientation, a closer examination of their intricate structures leads to varying geological interpretations. The concave-down geometry of R7 combined with its high-velocity features compellingly indicates its identity as a detachment fault (**Table 1**; see Discussion 5.1.1 for details). R8, characterized by its planar configuration and absence of significant velocity variations, is interpreted as a magmatic dike situated within the lower crust (**Table 1**). The interplay between the structures of R9 and R10 points towards them representing a volcanic edifice (**Table 1**). Notably, R9, which encapsulates high velocities and shares a parallel dip with R7, hints at the formation of a detachment fault along its stretch (**Table 1**).

In line with the interpretations for Segment 1, the upper unit (between the seafloor and the dotted pink line, **Figs. 4C-4D**), characterized by low velocities (< 4 km/s) and frequent fault penetrations, is interpreted as the upper crust, corresponding to the extrusive igneous layer of the oceanic crust. The lower unit (below the dotted pink line, **Figs. 4C-4D**), marked by high velocities (4.5-7 km/s), is interpreted as the lower crust, corresponding to the intrusive igneous layer of the oceanic crust. The sub-horizontal reflectors (R3) at the base of the lower crust are interpreted as the Moho.

In summary, the transition between the upper and lower crust, represented by the dotted pink line in **Figs. 4C-4D**, approaches close to the surface. This suggests that the upper crust within the NE-SW spreading valley is notably thin, accompanied by localized exhumation of the lower crust and/or mantle.

#### 4.2.3 Intra basement of southern ridge shoulder

The upper unit of the southern shoulder shows stronger reflections, while the lower unit has much lower amplitudes in the MCS image (**Fig. 4B**). At the NE of the southern shoulder (distance of 35-45 km), numerous high-amplitude, lateral-extending reflectors are observed at a depth of 6-8 s TWTT (R11, **Fig. 4B**). These strong reflectors (R11) intersect the NE-dipping reflectors (R4). The upper unit, where R11 and R4 occur, corresponds to low velocities (< 3 km/s, **Fig. 4D**), which is much thicker than the low-velocity unit in other domains of this profile.

At the SW of the southern shoulder (distance of 22-35 km), a nicely dome-shaped reflection can be observed at a distance of 22-35 km, a depth of 7-9 s TWTT (R12, **Fig.**

4B). The upper part of R12 reaches the seafloor at a distance of 30 km, and its lower part steeply dips to the SW, parallel to R7 and R9. Except for R12, the southern shoulder generally exhibits low-amplitude reflectors below the seafloor. R12 separates low velocities (< 3 km/s) from higher velocities, demonstrating similar features to R7 and R9 in the spreading valley.

The upper unit with weak reflections and low velocities (< 3km/s) is interpreted as the upper crust consisting of extrusive igneous rocks, while the lower unit with increased velocities (> 4.5 km/s in **Fig. 4D**) is interpreted as the lower crust (intrusive igneous rocks). The Moho reflectors are obscured at the southern ridge shoulder. At the NE of the southern shoulder (distance of 35-45 km), high-angle faults (R4) dipping to the NE offset the top basement, and numerous strong reflections within the upper crust (R11) are interpreted as sills related to magmatic intrusions (**Table 1**). At the SW of the southern shoulder, the dome-shaped structure with high velocities (R12) is similar to R7 in the spreading valley, and both are interpreted as OCCs associated with detachment faults (**Table 1**) (for further details see Discussion 5.1.1).

Overall, a rougher top basement and the extensive distribution of high velocity at shallow levels indicate a tectonic top basement (i.e., the OCCs) in Segment ②. These results suggest more intense tectonic activity in Segment ② (for further details see Discussion 5.4).

### 4.3 Segment ③: N-S spreading valley

4.3.1 Top basement

In the N-S spreading valley, an edifice with a 500-m relief exhibits high-amplitude reflectors dipping away from the peak near the seafloor (R13, **Fig. 5B**). The seafloor in the southwest of the edifice is mostly smooth (Smoo4, **Fig. 5B**) with occasional high-angle, SW-dipping reflectors (R14, **Fig. 5B**) that offset the seafloor. The seafloor becomes shallower at a distance greater than 100 km and is offset by parallel-dipping R15 to the NE. At the northern ridge, the seafloor steps up to the NE, shallowing from 6.5 s TWTT (4.8 km) to 5.5 s TWTT (4 km) (Step1, **Fig. 5B**). SW-dipping, high-angle reflectors (R16) are densely distributed. A thin layer of parallel reflectors is observed at a distance of 85-95 km (green sequence, **Fig. 5C**).

In line with Segments ① and ② interpretations, shallow-penetrated, high-angle dipping reflectors R14, R15, and R16 (**Fig. 5B**) are interpreted as high-angle normal faults (**Table 1**). R16 exhibits large vertical displacements, resulting in a terraced seafloor progressively shallower towards the southern shoulder. The thin sequence beneath Smoo4 (**Fig. 5B**) is interpreted as sediments with a thickness of less than 100 m (green sequence, **Fig. 5C**) (**Table 1**).

Observations from profile B-B' align with the findings from profile A-A', highlighting a set of high-angle normal faults with contrasting dip orientations (**Figs. 5F-5G**). The upper unit, penetrated by these faults, exhibits low velocities (**Fig. 5H**). Such observations concur with those from Segment ③ in profile A-A'. Together, they emphasize that N-S seafloor spreading was primarily dominated by high-angle normal faulting.

4.3.2 Intra basement

Underneath the small edifice, high-amplitude, medium continuous reflectors R13 parallel the seafloor, forming a constructive structure (**Fig. 5B**). R14 and R15 penetrate 0.5-s TWTT below the seafloor in the spreading valley, where velocities remain low (< 4km/s, **Fig. 5D**). However, at the northern ridge shoulder, R16 penetrates deeply (>2 s TWTT below the seafloor) and cuts three sets of high-amplitude, sub-horizontal reflectors (R20) at a depth of 6–7.5 s TWTT. The sequences bounded by the seafloor and R20 thicken to R16 and rotate clockwise. The distributions of R16 and R20 correspond to the upper unit where velocities are < 4.5 km/s.

At a depth of 8.5 s TWTT, a set of sub-horizontal, moderate amplitude reflectors with wavy patterns is observed (R17, **Fig. 5B**). Separated by R17, the lower unit exhibits a lower amplitude reflection than the upper unit near the seafloor. Consistently, a sharp increase in interval velocities (> 4.5 km/s, **Fig. 5D**) can be observed when it reaches the wavy reflectors. High-angle, SW-dipping reflectors, R18 and R21, are observed at a depth of 8.5 – 9.5 s TWTT (**Fig. 5B**) without significant velocity anomalies (**Fig. 5D**). Weak, discontinuous reflectors R19 correspond to a sharp increase of velocities to > 7 km/s at a depth of 9.5 s TWTT (**Fig. 5D**).

Based on the constructive structure evident in the MCS image, R13 is interpreted as a volcanic edifice (**Table 1**). Both R18 and R21 display steep dips without any notable velocity anomalies and are thus interpreted as magmatic dikes (**Fig. 5B, Table 1**).

Similarly, R17, exhibiting seismic reflection features similar to R18 and R21, is believed to be associated with the development of magmatic sills at the transition zone between the upper and lower crust (**Fig. 5C**). This interpretation is reinforced by an observed increase in velocities (**Fig. 5D**). The Moho is identified at a depth of 9.5 s TWTT, represented by R19 (**Figs. 5B-5D**).

In summary, the upper crust within Segment ③ exhibits a progressive thickening from the spreading valley towards the northern shoulder, corresponding to the step-shaped seafloor (**Fig. 5E**). However, the thickness of the lower crust remains consistent (**Fig. 5E**). Such crustal configurations imply a less intense tectonic activity in Segment ③, leading to the formation of a magmatic top basement.

## 5. Discussion and Implication

Seismic observations reveal a transition from a normal oceanic crust, characterized by consistent seismic reflection patterns and uniform thickness (Segments ① and ③), to a highly tectonized oceanic crust, which is distinguished by its rough tectonic top basement and a widespread presence of high velocities at shallow depths (Segment ②). In this discussion, we delve deeper into (1) the interplay between tectonic faulting and magmatism, (2) the progression of detachment faulting, (3) variations in fault patterns and their implications for magma supply during spreading, and (4) a comparison between slow-spreading ridges in back-arc basins (e.g., WPB) and open oceans (e.g., MAR and SWIR).

### 5.1 Sequential detachment faults

5.1.1 Identification of detachments and OCCs

As outlined in Section 4.2.2, DF2 shows steep dips of 62° in the rooting zones, which progressively flatten towards the seafloor, forming a concave-down geometry (**Fig. 4E**). Integrated with the high velocities observed in the footwall of DF2 (**Fig. 4D**), we interpret the tectonic movement associated with DF2 leads to the uplift and exhumation of the lower crust and/or mantle materials, resulting in the formation of OCC2 (**Fig. 4C**).

Similarly, evident high velocities (**Fig. 4D**) and concave-down geometries (**Fig. 4C**) characterize the footwalls of DF1 and DF3. The spatial distribution of these footwalls aligns with the structural elevations as mapped by bathymetry (**Figs. 2B and 4E**). Additionally, these faults terminate at the Moho depth (**Figs. 4C-4E**). Such insights indicate that the exhumation of gabbro, possibly accompanied by serpentinization, occurred at the footwalls of DF1 and DF3, thereby forming OCC1 and OCC3 (**Fig. 4C**). Drawing upon these observations, the seismic profile A-A’ unveils three sets of detachments: DF1, DF2, and DF3, each exhibiting a consistent SW-dipping orientation. Notably, DF1 is situated on the southern ridge shoulder, while DF2 is located within the NE-SW spreading valley, and DF3 correlates with the structural high situated between the NE-SW and N-S valleys.

5.1.2 Detachment faults and normal faults

The hanging wall of DF2 shows a large-scale anticline with clockwise rotation (**Figs.**

6B and 6D), forming the NE side of the southern ridge shoulder. In the hanging wall of DF2 (distance of 32-42 km), an array of NE-dipping normal faults (R4, Fig. 4B) accompanied by extrusive sequences (yellow sequences, Figs. 4C and 6A) exhibits an anticlockwise rotation of each panel (Fig. 6B). These structural architectures suggest that the hanging wall of DF2 underwent a large-scale clockwise rotation, compensated by the smaller-scale "bookshelf" structures undergoing anticlockwise rotation (Fig. 6). Such observations indicate that these secondary normal faults in the hanging wall of the detachment fault exerted a minimal impact on the primary architectures of the oceanic crust.

In the footwall of DF2, a series of SW-dipping normal faults (R6, Fig. 4B) offset the exhumed footwall (Figs. 4 and 6). Such observations indicate at least two stages of tectonic faulting during the latest NE-SW spreading: initial detachment faulting followed by high-angle faulting (Figs. 4 and 6). It is plausible that these normal faults offset DF2 function as conduits for magma migration. This mechanism might have played an important role in the termination of the detachment faulting, a topic explored in greater depth in Section 5.2.2.

5.1.3 Sequential development of detachment faults

In the seismic profile under examination, DF1 and DF2 show a distinctive dome-shaped fault geometry. DF1 is located on the southern ridge shoulder, while DF2 is located in the NE-SW spreading valley. Due to its closer proximity to the latest spreading axis, DF2 is associated with the formation of a younger oceanic crust. In comparison, the footwall of DF1 located on the southern shoulder is much shallower than the footwall of DF2, as manifested by the 1 km relief detailed in **Fig. 4E**). As delineated in Section 5.1.2, the rotation of the DF2's hanging wall formed the NE side of the southern shoulder, potentially augmenting the uplift of DF1's footwall. Consequently, it can be inferred that the older detachment fault, DF1, experienced rotational adjustments influenced by the evolution of its successor, DF2.

In contrast, DF3 displays a steeper dip, devoid of the archetypical dome geometry evident in DF1 and DF2. A set of sub-parallel reflectors with constructive features, labeled R10 (**Fig. 4B**), are observed at shallow levels, suggesting a volcanic edifice in proximity to DF3. Moreover, a thin layer of extrusives postdating DF2 overlays the footwall of DF2, as elaborated in Discussion 5.2.2. Given that the distinctive dome shape in the footwall of DF2 while DF3 shows steep angles, we interpret DF2 as an older detachment fault subsequently overlaid by DF3, a steep-dipping, younger detachment fault.

Steep-dipping DF3 is indicative of the initial detachment faults in the WPB that were initiated at high angles. This observation agrees with the kinematic models proposed for detachment fault systems, which posit that initial ridge flank faults initiate as steep inclinations, approximately 65°, before rotating to shallower angles (Cannat et al., 1997; MacLeod et al., 2009). Based on this, it is postulated that in the WPB, the initial regime of the CBF was characterized by a series of opposite-dipping high-angle faults (**Fig. 7A**). Subsequently, one of the valley-wall normal faults started to rotate, evolving into a mature detachment fault with a low-angle surface (**Fig. 7B**).

In summary, the trajectory of detachment fault development encompasses three distinctive fault sets, namely DF1, DF2, and DF3. These detachments systematically evolve from the southern ridge shoulder (DF1) to the spreading valley (DF2 and DF3). Interestingly, DF3, representing a younger detachment system, appears to overlay DF2, as explored in depth in Discussion 5.2.2.

**5.2 Relationships between magmas and faults**

5.2.1 Magmatism in the hanging wall of a detachment fault

As described in Sections 4.2.1 and 5.1.2, the top basement on the southern shoulder (orange lines, **Fig. 6B**) manifests as a rollover anticline and extrusive sequences on the hanging wall of DF2 (orange sequences, **Figs. 4C and 6D**) display a subtle NE inclination. Such configuration suggests that the hanging wall of DF2 experienced a large-scale clockwise rotation (**Fig. 6D**). Nevertheless, this overarching rotation contrasts with more localized nuances observed within the top basement. Specifically, a smaller-scale anticlockwise rotation, characterized by the presence of yellow extrusive sequences (**Fig. 4C**) and NE-dipping, high-angle normal faults (R4, **Fig. 4B**), indicates the first-order clockwise rotation of DF2's hanging wall is compensated by a secondary-order anticlockwise rotation (**Figs. 4C, 6A-6B**).

Given these secondary normal faults (R4, **Fig. 4B**) in the hanging wall of DF2 exerted a minimal impact on the primary architectures of the oceanic crust, as discussed in Section 5.1.2, we suggest that the genesis of both the orange and yellow extrusive sequences largely coincided with the primary detachment activities associated with DF2, termed as syn-DF2 extrusion (**Figs. 4 and 6**).

Drilling down into the specifics, these NE-dipping normal faults (R4, **Fig. 4B**) cross-cut the magmatic sills (R11, **Fig. 4B**) within the yellow extrusive sequences (**Fig. 4C**). This configuration suggests that these high-angle faults potentially functioned as conduits, channeling magma to the overlaying yellow extrusive sequences. Thus, magmatic intrusions within the yellow sequences were temporally aligned with secondary high-angle normal faulting activities (**Figs. 4 and 6**).

Similarly, thin layers of extrusives also develop on the hanging wall of DF1, delineated by purple sequences at a distance of 20-30 km (**Fig. 4C**). These purple sequences dip towards DF1, indicating the extrusion occurred synchronously with detachments, i.e., syn-DF1 extrusion (**Fig. 4**).

#### 5.2.2 Magmatism in the footwall of a detachment fault

On the footwall of DF2, a thin layer of extrusive (pink sequences, **Figs. 4C and 6F**) shows a horizontal reflection pattern (**Fig. 6F**) and thickens to the high-angle normal faults (R6, **Fig. 4B**). Two potential scenarios can elucidate the timing of these pink extrusions (**Fig. 7**). In the first scenario, the extrusive sequence associated with the high-angle faulting emerges subsequent to the exhumation, forming a horizontal reflection pattern superimposed on the OCC (**Fig. 7C**). Conversely, the second scenario posits that magma extrusion occurs during exhumation and formation of the OCC. This synchronous occurrence would have resulted in the rotation of extrusive layers (reflections) (**Fig. 7D**).

Based on our analysis, the horizontal reflection pattern of pink extrusive sequences (**Fig. 6F**) aligns with the premises of scenario 1. Complementarily, insights from Section 5.1.2 elucidate that, within the footwall of DF2, the sequential progression from detachment faulting to high-angle faulting resonates with the assertion that extrusion related to high-angle faulting manifested post the exhumation cessation (**Fig. 7C**). Consequently, we propose that this extrusion event materialized subsequent to the completion of OCC development, a phenomenon we designate as post-DF2 extrusion (**Figs. 4, 6 and 7**). This extrusive event effectively encapsulated the previously exhumed tectonic top basement (**Fig. 7C**).

Notably, post-detachment extrusion has been proposed based on field observations in the Alps, the former oceanic domain (e.g., Coltat et al., 2020; Manatschal et al., 2023). Within the context of high-angle normal faulting, magma likely ascended via these steep faults, subsequently settling atop the detachment fault footwalls. This would have eventually overwhelmed the development of OCC, as suggested by Manatschal et al. (2011). Additional discourse on this topic can be found in Section 5.5. Our seismic interpretations support that the detachment faulting phase (or the prevalent OCC state) was superseded by a subsequent phase of syn- normal faulting magmatism, denoting the terminal phase of the OCC life cycle.

### 5.3 Evolution of a slow spreading in the eastern WPB

Drawing from our discussions on sequential detachment faulting and magmatism, we present an evolution model for the slow seafloor spreading in the eastern WPB (**Fig. 8**).

*Stage 1:* High-angle faulting and magmatic accretion

Prior to the initiation of detachment faulting, seafloor spreading took place with a high magma supply, as observed in the southwest ridge flank (Segment ①, **Fig. 4**). According to the kinematic model by Deschamps et al. (2002), seafloor spreading at this period had an N-S orientation, producing an oceanic crust of consistent thickness, with pronounced extrusive layers and shallow-penetrated high-angle normal faults (**Fig. 8A**). During this period, thick extrusives associated with high-angle faulting at the ridge shoulders were formed (Segment ③ and profile B-B', **Fig. 5**). The MOR then exhibited a pair of conjugate normal faults with contrasting dips (Segment ③ and profile B-B', **Fig. 5**), leading to a linear spreading axis accompanied by symmetric magmatic accretion (**Fig. 8A**). Subsequently, the orientation of the seafloor spreading transitioned from N-S to NE-SW (**Fig. 8B**), as inferred from bathymetric cross-cutting relationships (**Fig. 2**, after Deschamps et al., 2002).

*Stage 2:* Detachment faulting and OCC development

As magma supply diminished, plate separation became concentrated on one of the dominant high-angle normal faults, subsequently known as DF1 (**Fig. 8B**). The future DF1 started its rotation, bringing the lower crust and mantle lithosphere to the seafloor, which led to the emergence of detachment fault DF1 and the mature OCC1 (**Fig. 8C**). As seafloor spreading continued, plate separation migrated closer to the spreading axis, focusing on a new normal fault, the future DF2. When future DF2 started to roll over, materials from the deeper crust and mantle ascended, resulting in footwall exhumation and the formation of a younger OCC2 (**Fig. 8D**). The younger DF2 developing on the footwall of the older DF1 indicates the NE-SW spreading axis migrating to the NE (**Fig. 8D**).

*Stage 3*: High-angle faulting and post-exhumation magma extrusion

Following the full exhumation of deep materials on the seafloor, high-angle normal faults initiated and offset the top basement (**Fig. 8E**). Simultaneously, magma utilized these normal faults as pathways, forming a thin extrusive layer (**Fig. 8E**). This extrusion occurred after OCC2 ceased, leading to an OCC2 sealed by extrusives (**Fig. 8E**), i.e., the pink extrusives observed on the footwall of OCC2 (**Figs. 4C and 6 F**). Meanwhile, a high-angle normal fault started to rotate, evolving into an early-stage detachment fault with steep angles, as observed in DF3 (**Fig. 4C**). Prior to the migration of OCC3 to the spreading axis, seafloor spreading ceased, forming an infant detachment fault DF3 with steep angles (**Fig. 8F**).

It is noted that Deschamps et al. (2002) suggested an initial N-S seafloor spreading direction in the WPB that terminated around 30 Ma. This was followed by an amagmatic extension in the NW-SE direction, accompanied by dextral strike-slip faulting along the CBF during 30-26 Ma. Our findings propose that this latest NE-SW orientation was not entirely devoid of magma. Instead, it was magma-poor, indicated by a thin layer of extrusives in the NE-SW axial valley (**Fig. 8G**).

### 5.4 Fault pattern, magmatic budget, and magmatism-tectonics interaction

The alternation between magmatic and tectonic top basements along profile A-A' suggests that the oceanic crust in the eastern WPB is generated by an interaction between magmatism and tectonic faulting. When magmatism dominated seafloor spreading, the oceanic crust exhibited a smooth top basement and shallow-penetrated high-angle faults (Segments ① and ③). Conversely, when tectonic faulting prevailed, the oceanic crust showed a rough top basement, variable extrusive thickness, and mantle exhumation at OCCs (Segment ②).

Fault patterns and magmatic budgets underwent significant changes during the evolution of the MOR. In the initial phase, the system was defined by a set of conjugated high-angle normal faults (**Figs. 8A-8B, 9A and 9D**), indicating diffusive and de-localized extensional strain. With the interaction between high-angle faulting and magmatic addition, the seafloor spreading was controlled by a pure-shear extension, generating a symmetric pattern and a continuous magmatic top basement (**Figs. 8A-8B**).

As magma waned, fault displacement increased (via rotation) to compensate for the diminished magmatic component of spreading, and the magmatic crustal layer became highly heterogeneous. With the development of detachment faulting, deep gabbro and serpentinized mantle uplifted and exhumed to a shallower depth (**Figs. 8C, 9B**). At this time, strain localized on the active detachment fault (DF1), and the seafloor spreading was controlled by an asymmetric, simple-shear extension. This led to the formation of an OCC, producing a tectonic top basement that disrupted the continuity of the previous magmatic top basement (**Figs. 8C**).

Continued seafloor spreading, paired with a low magma budget, led to the development of a younger detachment fault (DF2), with strain localized on the active DF2 (**Fig. 8D**). During this phase, the tectonic top basement interrupted the magmatic top basement in two distinct segments (**Fig. 8D**).

Upon OCC2's development, an increase in the magma budget was observed, marked by the extrusives covering OCC2 (pink sequences in **Figs. 4C, 6F, and 8E**). This led to a shift in the local thermal structures of the infant OCC2 from low to high heat flow, overwhelming and terminating the young detachment system DF2. The sealing of extrusives on the OCC2 created a magmatic basement atop the DF2, leading to the restoration of symmetric, pure-shear extension control over seafloor spreading in the most recent high-angle faulting stage (**Fig. 8E**).

In summary, a transition occurs from the southwest ridge flank (far from the latest spreading axis) to the NE-SW spreading valley (near the latest spreading axis), where fault patterns shift from symmetric normal faults to asymmetric detachment faults, and ultimately revert back to symmetric normal faults (**Figs. 8 and 9**). This spatial change of fault patterns is consistent with the variation of magma supply, thus suggesting a thermal structure evolves from a magma-rich state during pure-shear extension, to a magma-poor state during simple-shear extension, and a return to a magma-rich state during pure-shear extension. Given the 30° angle between the MCS profile and the spreading axis, these findings also indicate an along-strike variation in thermal-mechanical structure (**Fig. 9**).

### 5.5 Comparison to MAR and SWIR

We observe three sets of detachment faults at the spreading center of the WPB, all dipping to the same directions (**Fig. 9**). The pattern of detachment faults dipping to the same direction is similar to the OCCs at the MAR (Cannat et al., 1997; MacLeod et al., 2009). However, this separated detachment fault pattern markedly contrasts with the cross-cut detachment faults seen at the ultraslow SWIR (Sauter et al., 2013). Additionally, the extensive syn-tectonic extrusion in the WPB is also contracted to the nearly amagmatic structure of the SWIR (Sauter et al., 2013).

Extrusives in the hanging wall of detachment faults are common in seafloor spreading systems, as observed in the volcanic zones at 26° N at the MAR (DeMartin et al., 2007). However, reports of extrusives in the footwall of detachment faults have so far been limited to regions such as the Alps, the former oceanic domain (Coltat et al., 2020; Manatschal et al., 2023). We propose that extrusives covering OCC are consistent with the conceptual model of an OCC life cycle in which increased magmatism would overwhelm and terminate the development of the OCC (Manatschal et al., 2011). This is consistent with our observations of the creation of an infant OCC, i.e. OCC3, near the latest spreading axis (**Figs. 8 and 9**).

As proposed in the other slow and ultraslow MORs, a seafloor spreading axis is usually characterized by separated large-scale detachment faulting (e.g., MAR with low magmatic budget) or cross-cut detachment faulting (e.g., SWIR with extremely low magmatic budget). Variations in magmatic budget and changes from tectonic-dominated to magmatic-dominated spreading are usually suggested to be controlled by spreading rates (e.g., Buck et al., 2005; Liu and Buck, 2020; Tucholke et al., 2008). However, recent studies show the transition from magmatic-dominated to tectonic-dominated spreading is rather a matter of melt supply (Cannat et al., 2019; Chen et al., 2022; Fan et al., 2021). In this study, we further demonstrate that the fault pattern and magma supply changes over a distance of ~70 km along strike and thus are unlikely to solely reflect changes in plate divergence. We propose that along-strike strain de-localization (magma-dominated) and localization (tectonic-dominated) can occur simultaneously at the same spreading rates.

## 6. Conclusions

Our study of the eastern MOR of the WPB presents the variations in fault patterns and magma supply across ridge and along strike directions. Our findings reveal that the final stage of slow spreading in the WPB experienced a cycle of symmetric magma-rich accretion, asymmetric magma-poor spreading, and magmatism overwhelming the development of OCCs.

The relationship between high-angle normal faults and detachment faults indicates a transition from strain de-localization (pure-shear) to localization (simple-shear), which is closely linked to magma waning. The pure-shear stage is characterized by symmetric high-angle faulting with certain amounts of extrusives, leading to a magmatic top basement, whereas the simple-shear stage corresponds to the development of detachment faults with limited and localized extrusives, leading to a tectonic top basement.

In addition to two mature OCCs with dome-shaped fault geometries, we also identified an infant OCC within the axial valley. Increased magma supply to the exhumed footwall terminated the exhumation of the OCC, thus forming a mature OCC covered by a thin layer of extrusives. Mature and infant OCCs in the WPB represent different genetic stages in the life cycle of a detachment system. The infant stage of an OCC is challenging to observe on the seafloor since it is not fully exhumed. Therefore, it is plausible that more infant OCCs can be reported when more high-resolution seismic data are available from slow and ultraslow MORs.

Previous studies explained the formation of OCCs based on across-ridge structures. We observe a combination of tectonic- and magmatic-dominated segments along strike. This observation suggests that, even within the same spreading rate range, the spreading mode can be determined by strain localization (magmatism concentration) and strain de-localization (magmatism de-concentration) instead of solely depending on the changes in spreading rates and the associated melt budget.

## Acknowledgments

Funding: This work was supported by the National Natural Science Foundation of China (No. 42276082, No. 91858214, and No. 42025601), Scientific Research Fund of the Second Institute of Oceanography, MNR (No. QNYC2301), Leading Talents in Scientific and Technological Innovation Project of Zhejiang Province (No. 2019R52034).

Data and materials availability: Bathymetric data are from (Tozer et al., 2019), available at https://topex.ucsd.edu/WWW_html/srtm15_plus.html, free-air gravity anomaly (https://topex.ucsd.edu/pub/global_grav_1min/), and magnetic anomaly (https://www.ngdc.noaa.gov/geomag/emag2.html) are individually extracted from global grids. Uninterpreted MCS image datasets are available at https://doi.org/10.5281/zenodo.8437090. Maps were constructed by using Generic Mapping Tools (GMT) version 6 (Wessel et al., 2019), available at https://www.genericmapping-tools.org/.

## References

Arculus, R.J., Gurnis, M., Ishizuka, O., Reagan, M.K., Pearce, A., Sutherland, R., 2019. How to create new subduction zones: A global perspective. Oceanography 32, 160–174.

Behn, M.D., Ito, G., 2008. Magmatic and tectonic extension at mid-ocean ridges: 1. Controls on fault characteristics. Geochemistry, Geophys. Geosystems 9.

Bell, R.E., Buck, W.R., 1992. Crustal control of ridge segmentation inferred from observations of the Reykjanes Ridge. Nature 357, 583–586.

Buck, W.R., Lavier, L.L., Poliakov, A.N.B., 2005. Modes of faulting at mid-ocean ridges. Nature 434, 719–723.

Cann, J.R., Blackman, D.K., Smith, D.K., McAllister, E., Janssen, B., Mello, S., Avgerinos, E., Pascoe, A.R., Escartin, J., 1997. Corrugated slip surfaces formed at ridge–transform intersections on the Mid-Atlantic Ridge. Nature 385, 329–332.

Cannat, M., Lagabrielle, Y., Bougault, H., Casey, J., de Coutures, N., Dmitriev, L., Fouquet, Y., 1997. Ultramafic and gabbroic exposures at the Mid-Atlantic Ridge: Geological mapping in the 15 N region. Tectonophysics 279, 193–213.

Cannat, M., Mével, C., Stakes, D., 1991. Stretching of the deep crust at the slow-spreading Southwest Indian Ridge. Tectonophysics 190, 73–94.

Cannat, M., Sauter, D., Lavier, L., Bickert, M., Momoh, E., Leroy, S., 2019. On spreading modes and magma supply at slow and ultraslow mid-ocean ridges. Earth Planet. Sci. Lett. 519, 223–233. https://doi.org/10.1016/j.epsl.2019.05.012

Cannat, M., Sauter, D., Mendel, V., Ruellan, E., Okino, K., Escartin, J., Combier, V., Baala, M., 2006. Modes of seafloor generation at a melt-poor ultraslow-spreading ridge. Geology 34, 605–608.

Chen, J., Olive, J.-A., Cannat, M., 2022. Thermal Regime of Slow and Ultraslow Spreading Ridges Controlled by Melt Supply and Modes of Emplacement. J. Geophys. Res. Solid Earth 127, e2021JB023715. https://doi.org/https://doi.org/10.1029/2021JB023715

Chen, Y., Morgan, W.J., 1990. Rift valley/no rift valley transition at mid-ocean ridges. J. Geophys. Res. Solid Earth 95, 17571–17581.

Coltat, R., Branquet, Y., Gautier, P., Boulvais, P., Manatschal, G., 2020. The nature of the interface between basalts and serpentinized mantle in oceanic domains: Insights from a geological section in the Alps. Tectonophysics 797. https://doi.org/10.1016/j.tecto.2020.228646

DeMartin, B.J., Sohn, R.A., Canales, J.P., Humphris, S.E., 2007. Kinematics and geometry of active detachment faulting beneath the Trans-Atlantic Geotraverse (TAG) hydrothermal field on the Mid-Atlantic Ridge. Geology 35, 711–714.

Deschamps, A., Lallemand, S., 2002. The West Philippine Basin: An Eocene to early Oligocene back arc basin opened between two opposed subduction zones. J. Geophys. Res. Solid Earth 107, EPM 1-1-EPM 1-24. https://doi.org/10.1029/2001jb001706

Deschamps, A., Okino, K., Fujioka, K., 2002. Late amagmatic extension along the central and eastern segments of the West Philippine Basin fossil spreading axis. Earth Planet. Sci. Lett. 203, 277–293. https://doi.org/10.1016/S0012-821X(02)00855-5

Ding, W., Zhu, R., Wan, B., Zhao, L., Niu, X., Zhao, P., Sun, B., Zhao, Y., 2023. Geodynamic processes of the southeastern Neo-Tethys Ocean and the formation mechanism of the curved subduction system in Southeast Asia. Sci. China Earth Sci. 66, 703–717.

Dix, C.H., 1955. Seismic velocities from surface measurements. Geophysics 20, 68–86.

Fan, Q., Olive, J., Cannat, M., 2021. Thermo-mechanical state of ultraslow-spreading ridges with a transient magma supply. J. Geophys. Res. Solid Earth 126, e2020JB020557.

Hall, R., 2012. Late Jurassic-Cenozoic reconstructions of the Indonesian region and the Indian Ocean. Tectonophysics 570–571, 1–41. https://doi.org/10.1016/j.tecto.2012.04.021

Hall, R., 2002. Cenozoic geological and plate tectonic evolution of SE Asia and the SW

Pacific: computer-based reconstructions, model and animations. J. Asian Earth Sci. 20, 353–431.

Hansen, L.N., Cheadle, M.J., John, B.E., Swapp, S.M., Dick, H.J.B., Tucholke, B.E., Tivey, M.A., 2013. Mylonitic deformation at the Kane oceanic core complex: Implications for the rheological behavior of oceanic detachment faults. Geochemistry, Geophys. Geosystems 14, 3085–3108.

Hilde, T.W.C., Lee, C.-S., 1984. Origin and evolution of the West Philippine Basin: a new interpretation. Tectonophysics 102, 85–104.

Howell, S.M., Olive, J.-A., Ito, G., Behn, M.D., Escartin, J., Kaus, B., 2019. Seafloor expression of oceanic detachment faulting reflects gradients in mid-ocean ridge magma supply. Earth Planet. Sci. Lett. 516, 176–189.

Huismans, R.S., Beaumont, C., 2003. Symmetric and asymmetric lithospheric extension: Relative effects of frictional-plastic and viscous strain softening. J. Geophys. Res. Solid Earth 108.

Ishizuka, O., Taylor, R.N., Ohara, Y., Yuasa, M., 2013. Upwelling, rifting, and age-progressive magmatism from the Oki-Daito mantle plume. Geology 41, 1011–1014. https://doi.org/10.1130/G34525.1

Lavier, L.L., Buck, W.R., Poliakov, A.N.B., 1999. Self-consistent rolling-hinge model for the evolution of large-offset low-angle normal faults. Geology 27, 1127–1130.

Lin, J., Purdy, G.M., Schouten, H., Sempere, J.-C., Zervas, C., 1990. Evidence from gravity data for focusedmagmatic accretionalong the Mid-Atlantic Ridge. Nature 344, 627–632.

Liu, Z., Buck, W.R., 2020. Global Trends of Axial Relief and Faulting at Plate Spreading Centers Imply Discrete Magmatic Events. J. Geophys. Res. Solid Earth 125, 1–20. https://doi.org/10.1029/2020JB019465

MacLeod, C.J., Escartin, J., Banerji, D., Banks, G.J., Gleeson, M., Irving, D.H.B., Lilly, R.M., McCaig, A.M., Niu, Y., Allerton, S., 2002. Direct geological evidence for oceanic detachment faulting: The Mid-Atlantic Ridge, 15 45′ N. Geology 30, 879–882.

MacLeod, C.J., Searle, R.C., Murton, B.J., Casey, J.F., Mallows, C., Unsworth, S.C., Achenbach, K.L., Harris, M., 2009. Life cycle of oceanic core complexes. Earth Planet. Sci. Lett. 287, 333–344. https://doi.org/10.1016/j.epsl.2009.08.016

Manatschal, G., Chenin, P., Ulrich, M., Petri, B., Morin, M., Ballay, M., 2023. Tectono-magmatic evolution during the extensional phase of a Wilson Cycle: a review of the Alpine Tethys case and implications for Atlantic-type margins. Ital. J. Geosci. 142, 5–27.

Manatschal, G., Sauter, D., Karpoff, A.M., Masini, E., Mohn, G., Lagabrielle, Y., 2011. The Chenaillet Ophiolite in the French/Italian Alps: An ancient analogue for an Oceanic Core Complex? Lithos 124, 169–184. https://doi.org/10.1016/j.lithos.2010.10.017

Olive, J.-A., Behn, M.D., Tucholke, B.E., 2010. The structure of oceanic core complexes controlled by the depth distribution of magma emplacement. Nat. Geosci. 3, 491–495.

Reston, T.J., McDermott, K.G., 2011. Successive detachment faults and mantle unroofing at magma-poor rifted margins. Geology 39, 1071–1074. https://doi.org/10.1130/G32428.1

Sauter, D., Cannat, M., Rouméjon, S., Andreani, M., Birot, D., Bronner, A., Brunelli, D., Carlut, J., Delacour, A., Guyader, V., MacLeod, C.J., Manatschal, G., Mendel, V., Ménez, B., Pasini, V., Ruellan, E., Searle, R., 2013. Continuous exhumation of mantle-derived rocks at the Southwest Indian Ridge for 11 million years. Nat. Geosci. 6, 314–320. https://doi.org/10.1038/ngeo1771

Schroeder, T., John, B.E., 2004. Strain localization on an oceanic detachment fault system, Atlantis Massif, 30 N, Mid-Atlantic Ridge. Geochemistry, Geophys. Geosystems 5.

Tian, X., Choi, E., 2017. Effects of axially variable diking rates on faulting at slow spreading mid-ocean ridges. Earth Planet. Sci. Lett. 458, 14–21.

Tozer, B., Sandwell, D.T., Smith, W.H.F., Olson, C., Beale, J.R., Wessel, P., 2019. Global Bathymetry and Topography at 15 Arc Sec: SRTM15+. Earth Sp. Sci. 6, 1847–1864. https://doi.org/10.1029/2019EA000658

Tucholke, B.E., Behn, M.D., Buck, W.R., Lin, J., 2008. Role of melt supply in oceanic detachment faulting and formation of megamullions. Geology 36, 455–458. https://doi.org/10.1130/G24639A.1

Wessel, P., Luis, J.F., Uieda, L., Scharroo, R., Wobbe, F., Smith, W.H.F., Tian, D., 2019. The Generic Mapping Tools Version 6. Geochemistry, Geophys. Geosystems 20, 5556–5564. https://doi.org/https://doi.org/10.1029/2019GC008515

Zhang, M., Di, H., Xu, M., Canales, J.P., Yu, C., Zhao, X., Wang, P., Zeng, X., Wang, Y., 2022. Seismic imaging of Dante's Domes oceanic core complex from streamer waveform inversion and reverse time migration. J. Geophys. Res. Solid Earth 127, e2021JB023814.

Zhang, Z., Dong, D., Sun, W., Zhang, G., 2022. Oligocene magmatic accretion and transtensional tectonics in the Central Basin Fault rift of the West Philippine back-arc basin: New insights from high-resolution multichannel seismic data. Mar. Pet. Geol. 141, 105703. https://doi.org/10.1016/j.marpetgeo.2022.105703

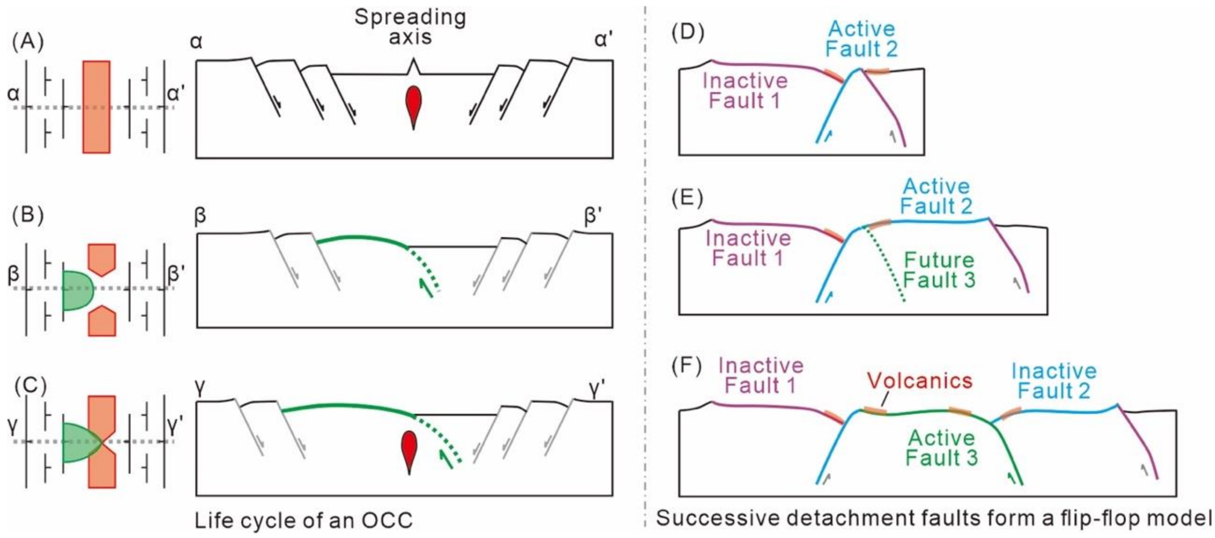


Figure 1. Kinematic models for the formation of new oceanic crust at slow and ultraslow spreading mid-ocean ridges (MORs). (A-C) Evolution of a detachment fault system and the associated life cycle of an oceanic core complex (OCC), after MacLeod et al. (2009). The left column presents a map view of observed seafloor geology, with the volcanic zone in red, the emerged detachment fault in green, and the other high-angle normal faults in black. The right column provides vertical cross-sections across the spreading axis. (D-F) “Flip-flop” model showing mantle exhumation on successive detachment faults (Reston and McDermott, 2011; Sauter et al., 2013). A comparison of these models highlights the close relationship between the type of fault pattern and melt supply, although it does not discuss the magma-deformation relationship in detail.

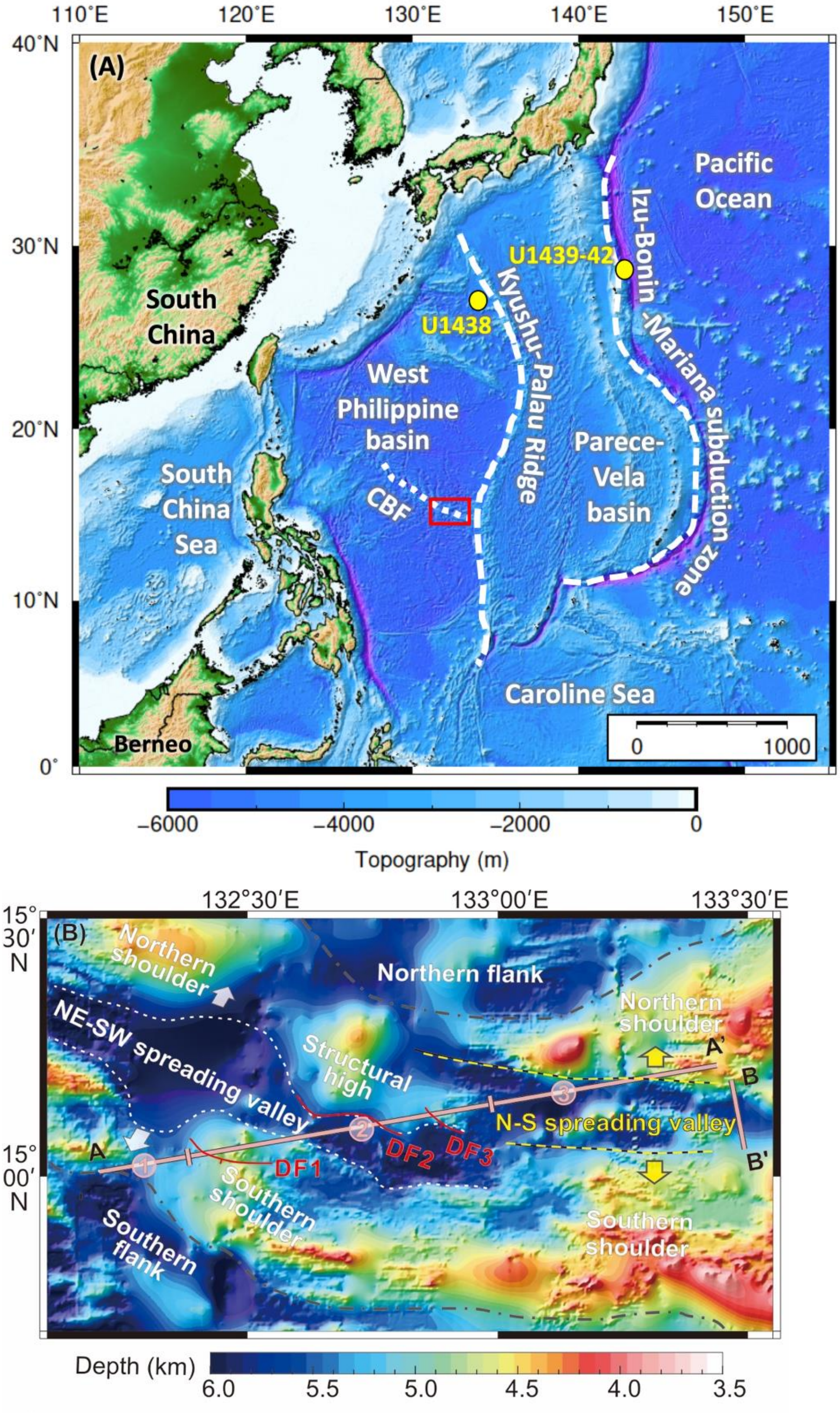


Figure 2. (A) Shaded view of the satellite-derived bathymetry of the Philippine Sea Plate and major seafloor features of the West Philippine Basin, drawing on data from Tozer et al. (2019). Red box identifies the location of (B). Yellow dots indicate the locations of IODP expeditions 351 (U1438) and 352 (U1439-42) drill sites (Arculus et al., 2019). (B) Zoom-in of the central basin fault (CBF, or the MOR) of the eastern WPB and the locations of the MCS reflection

profiles, A-A’ and B-B’. Profile A-A’ extends SW-NE oblique to the CBF and profile B-B’ extends NW-SE, situated at the eastern extremity of the N-S spreading valley. The CBF divides into N-S and NE-SW valleys due to the spreading reorientation from N-S to NE-SW (Deschamps et al., 2002). Two perpendicular profiles demonstrate variations of the slow spreading MOR over time and space.

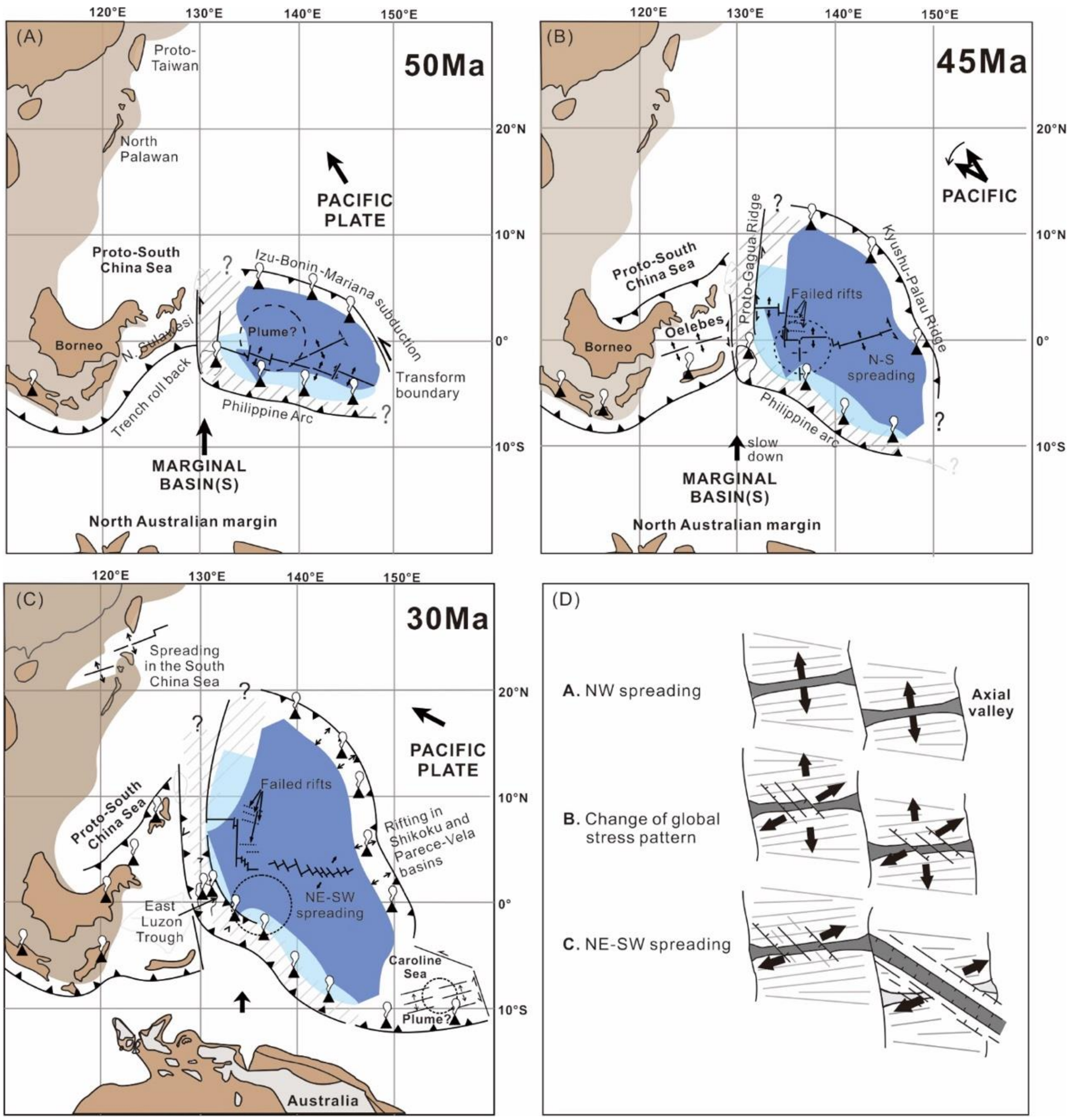


Figure 3 Evolution model of the West Philippine Basin at 50 Ma (A), 45 Ma (B), and 30 Ma (C), following the work of Deschamps and Lallemand (2002). (A) At 50 Ma, the seafloor was spreading in the N10W direction at a moderate rate (half-rate of 44 mm/a). (B) Around 45 Ma, a major plate reorganization EXTENDED from Southeast Asia through the western Pacific to Australia (e.g., Hall, 2002). In the WPB, the spreading rate decreased to a slow rate of 18 mm/a. (C) Around 33-30 Ma, a regional extension likely caused the latest spreading reorientation from N-S to NE-SW, evidenced by the NW-SE oriented spreading fabrics that intersect the E-W fabrics (Deschamps et al., 2002). (D) Sketch of extensional stress changes at different stages,

based on the topographic changes along the entire MOR of the WPB (after Deschamps et al., 2002).

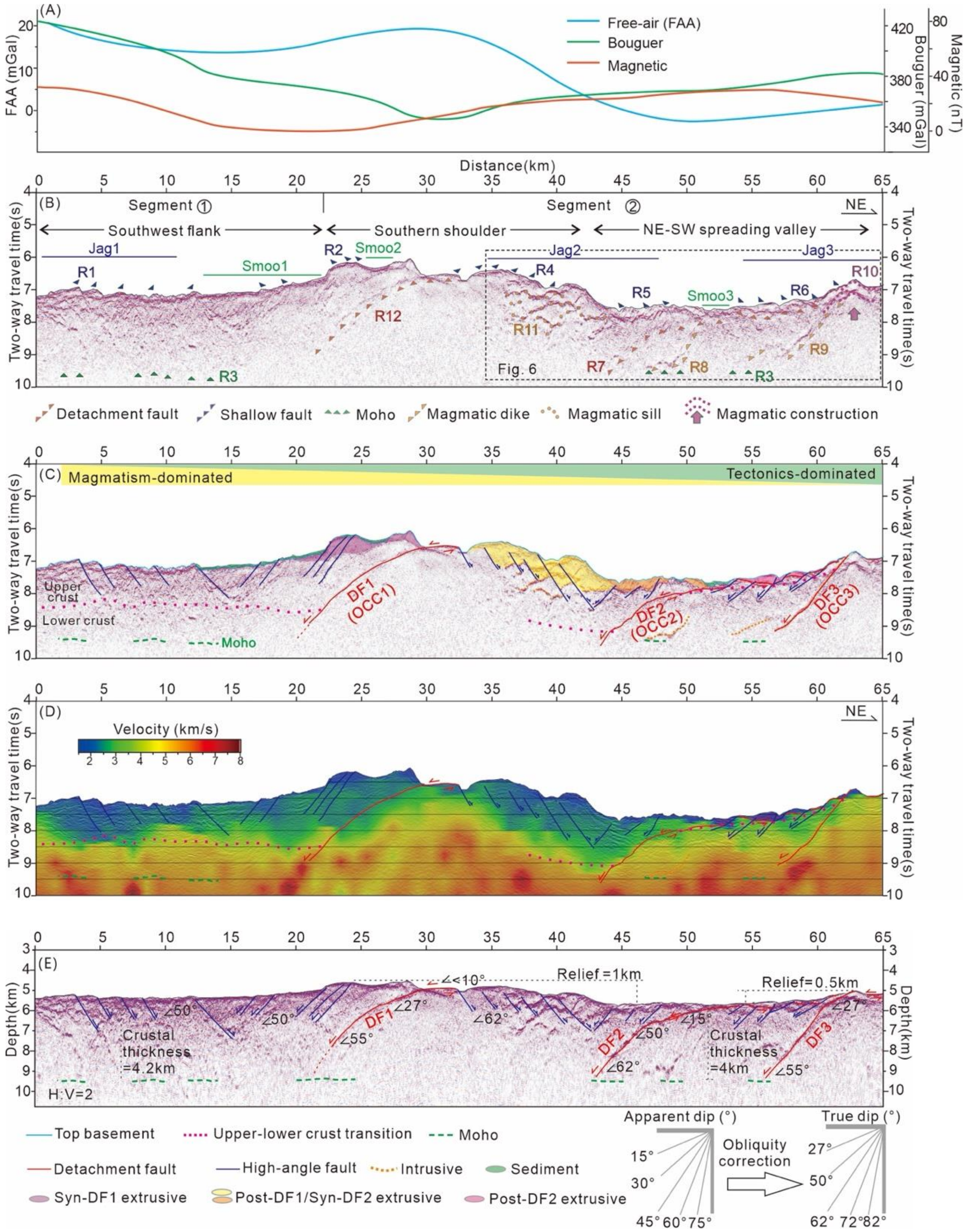


Figure 4. Segments ① and ② of the MCS profile A-A’, extending from the southwest ridge flank to the NE-SW spreading valley of the basin. (A) Extracted free-air gravity anomaly (FAA), Bouguer anomaly, and magnetic anomaly data from global grids. (B) MCS image displayed in the time domain. (C) Geological interpretation of the MCS profile. (D)

Superimposition of the MCS image and the interval velocity model along the profile. (E) Depth-migrated section with true dips of faults after a 60° obliquity correction. Segment ① exhibits a smooth top basement and uniform oceanic crust thickness, occasionally interrupted by high-angle faults, suggesting a magmatism-dominated spreading process. In contrast, segment ② features a rough top basement, high-angle faults (marked in blue), and low-angle surface expression faults (DF1, DF2, and DF3 in red). High velocities in the footwalls of the detachment faults hint at an upwelling of deep materials linked to detachment faulting, indicating a highly tectonised oceanic crust. The transition between the upper and lower crust is based on the velocity structure. The upper crust shows low velocities of < 4 km/s while the lower crust shows high velocities of >5 km/s. Refer to Section 5.2 for a discussion on syn- and post-detachment extrusions.

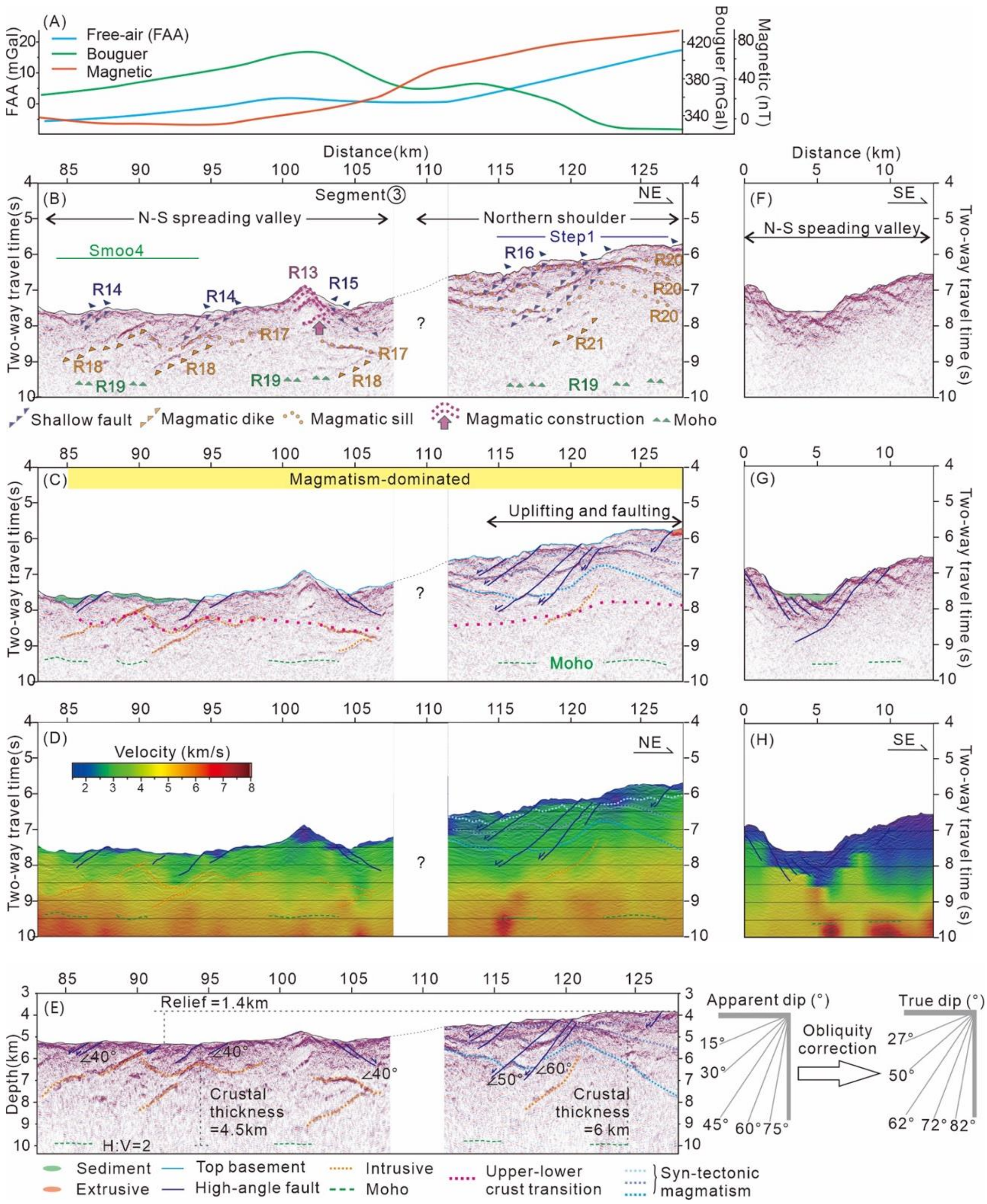


Figure 5. Segment ③ of profile A-A' (A-E) and profile B-B' (F-H) crossing the eastern end of the CBF formed by N-S spreading. (A) Free-air anomaly (FAA), Bouguer anomaly, and magnetic anomaly data along Segment ③ extracted from global grids. (B) MCS image of Segment ③ presented in the time domain. (C) Geological interpretation of Segment ③. (D) Superposition of Segment ③ and its interval velocity model. (E) Depth-migrated section of Segment ③ with true dips of faults after a 60° obliquity correction. (F) Seismic profile B-B'

perpendicular to profile A-A’. (G) Geological interpretation of profile B-B’. (H) Superposition of profile B-B’ and its velocity model. Segment ③ and profile B-B’ reveal that the eastern end of CBF is characterized by a highly faulted seafloor covered by a thick layer of syn- high-angle faulting extrusives with low velocities.

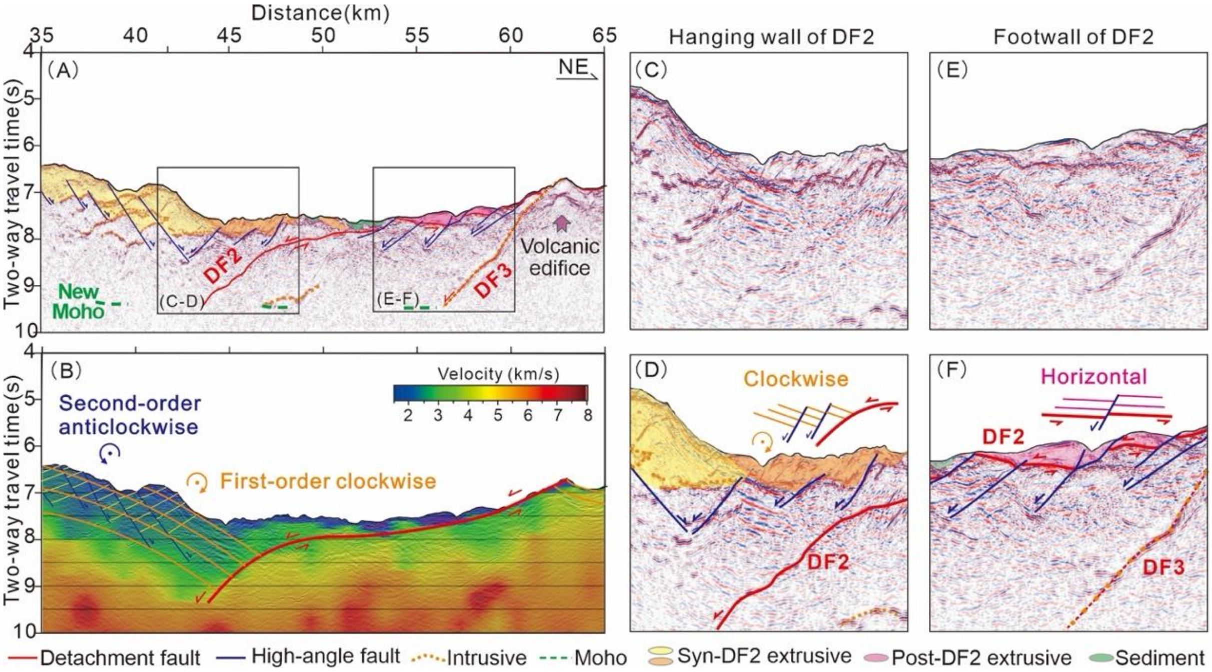


Figure 6 Zoom-in of the NE-SW spreading valley within the WPB. (A) MCS image represented in the time domain and its geological interpretation. DF2 shows a concave-down geometry with large horizontal displacements (~20 km). (B) Interval velocity model for the zoom-in and a simplified interpretation of the fault patterns. The top basement on the southern shoulder forms a rollover anticline (highlighted in orange), suggesting a large-scale clockwise rotation under the slipping of DF2; an array of NE-dipping normal faults (highlighted in blue) exhibiting a smaller-scale anticlockwise rotation. (C-D) Zoom-in of the extrusive in the hanging wall of DF2. The observed clockwise rotation indicates that these orange-colored extrusives are synchronous to the slipping of DF2. (E-F) Zoom-in of the horizontal extrusives in the footwall of DF2. Their thickening towards the high-angle faults, which offset the footwall of DF2, suggests that these pink-colored extrusives are synchronous to high-angle faulting but post-date detachment.

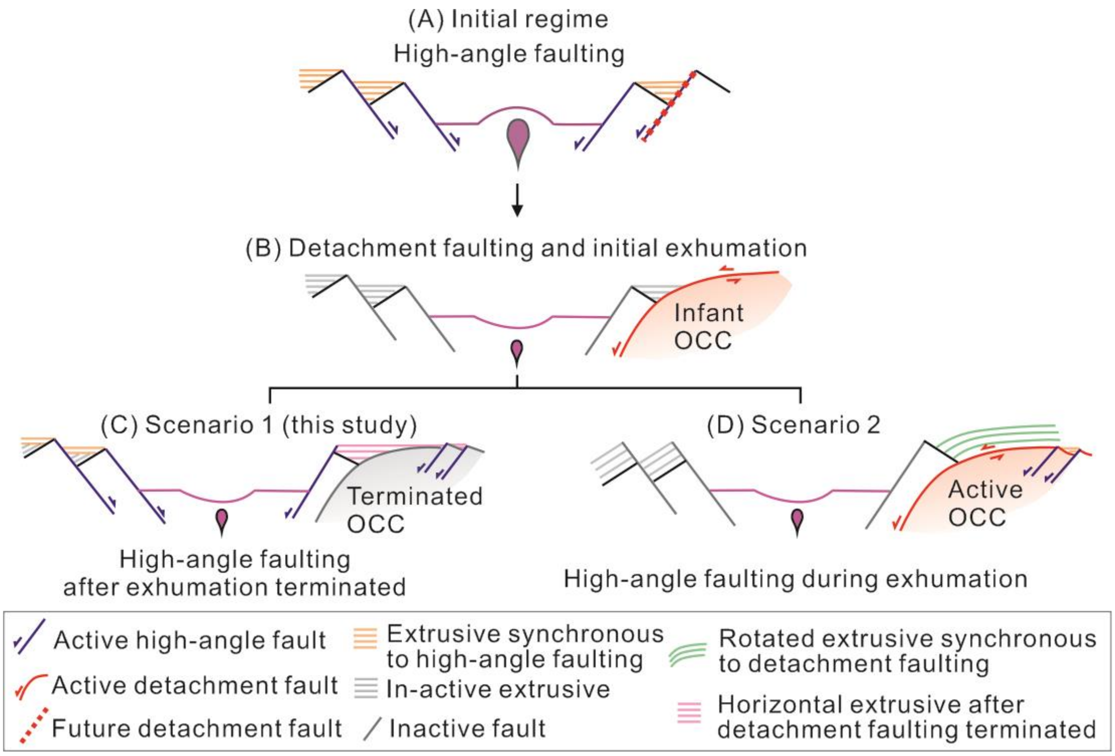


Figure 7. Illustrations showing the relationship between high-angle faulting, detachment faulting, and the magmatic extrusion during the life cycle of a detachment system. (A) Initial regime characterized by symmetric high-angle normal faulting. (B) One of the high-angle faults rotates, forming an early-stage detachment fault and its associated infant OCC. (C-D) Two potential scenarios for the relationship between high-angle faulting/extrusion and detachment faulting following (B). In scenario 1, magma extrusion associated with high-angle faulting occurs after exhumation, forming a horizontal reflection pattern covering the OCC (C). In scenario 2, extrusion and high-angle faulting take place during exhumation, resulting in the rotation of extrusive layers. Observations from this study align with scenario 1.

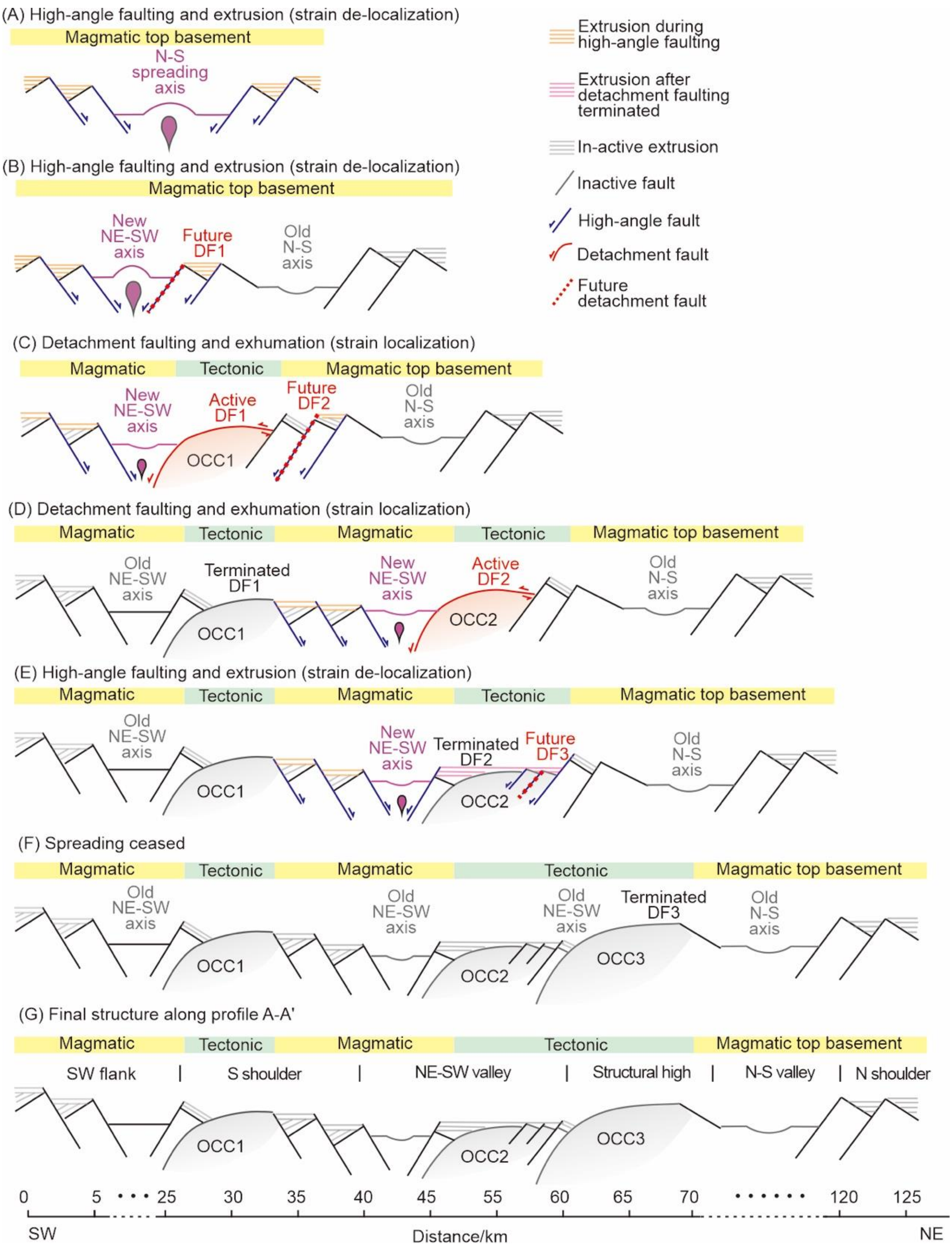


Figure 8. Models demonstrating the slow seafloor spreading processes of the WPB, achieved by the interaction between magmatism and tectonics in time and space domains. (A) N-S seafloor spreading was characterized by a straight ridge axis and symmetrical magmatic

accretion, generating a magmatic top basement. (B) Spreading direction transitioned from N-S to NE-SW, leading to a continuous generation of the magmatic top basement. (C) One of the normal faults rotated, forming a mature detachment fault DF1 and an associated OCC1. The development of OCC formed a tectonic top basement that interrupted the previous magmatic top basement. (D) Continuation of seafloor spreading instigated rotation in another proximal normal fault, forming the younger detachment DF2 and OCC2. The magmatic top basement was then disrupted by two tectonic basement segments. The development of the younger DF2 in the footwall of its predecessor, DF1, indicates the NE-ward migration of the NE-SW spreading axis. (E) Following full exhumation of OCC2, high-angle normal faults initiated, offsetting the top basement. These faults served as conduits for magma, facilitating the formation of a thin extrusive layer. Simultaneously, the future DF3 - another normal fault - was taking shape in the footwall of DF2. (F) Prior to the migration of OCC3 to the spreading axis, seafloor spreading ceased, forming an infant detachment fault DF3, characterized by its steep angles. (G) The final configuration exhibits an alternation between magmatic and tectonic top basements, as observed in the MCS profile A-A’.

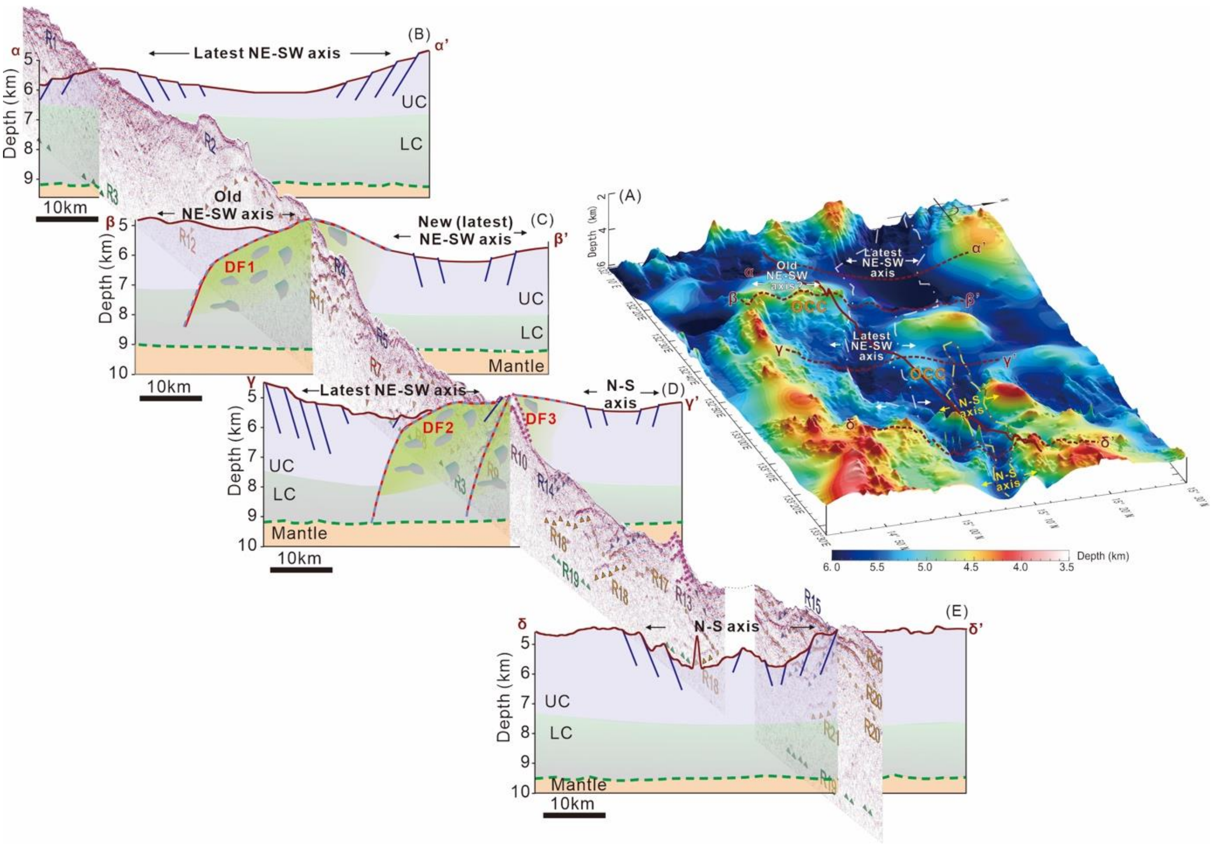


Figure 9. Perspective view of the 3D geological model for the study area depicted in (A) and the geological interpretation of four cross-sections (B-E) perpendicular to the spreading axes, based on profile A-A'. The solid red line in (A) indicates the location of profile A-A', and dashed red lines mark the locations of the cross-sections. The NE-SW spreading center is characterized by a wide valley with subtle gradients, flanked by OCCs. In contrast, the N-S spreading center presents as a narrow, steep valley. Cross-sections β-β' and γ-γ' display a sequence of three detachment faults (DF1, DF2, and DF3) dipping to the SW, indicating that the NE-SW spreading was dominated by tectonic faulting with limited magma supply (C-D). Cross-section δ-δ' shows high-angle normal faults with opposing dips, coupled with a uniform oceanic crust thickness and absence of OCC, suggesting a relatively abundant magma supply during the N-S spreading (E). Given the 30° angle between the MCS profile and the NE-SW spreading axes, the findings indicate an along-strike variation in the thermal-mechanical configuration.

Table 1 Groups of the seismic reflections, features, and their geological interpretation

| Group | Example | Reflection | Velocity | Interpretation |
|---|---|---|---|---|
| R1, R2, R4, R5, R6, R14, R15, R16 | 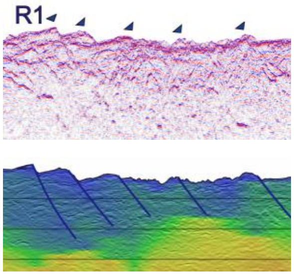  | Sub-planar, high-angle (>45°) dipping reflectors penetrating from jagged seafloor to shallow crustal levels (< 7 km in depth) | Low velocity at both hanging wall and footwall | High-angle normal fault |
| R7, R9, R12 | 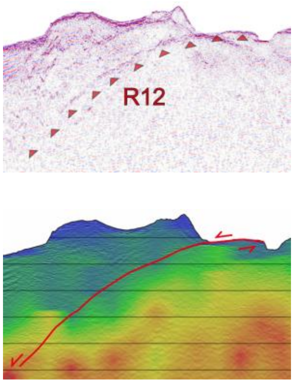  | A concaved-down geometry with gently dipping reflectors at a shallow level associated with moderate basement relief (0.5-1 km relief) and penetrating deep crustal levels (> 9 km in depth) | High-velocity at footwall | Detachment fault |
| R8, R11, R17, R18, R20, R21 | 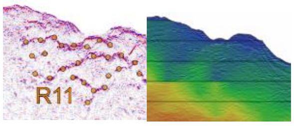  | Irregular shape, high-amplitude reflectors | No significant velocity anomaly | Magmatic sill or dike |
| R10, R13 | 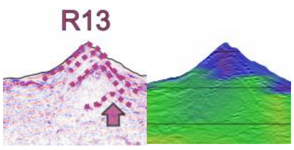  | High-amplitude, parallel reflectors showing constructive structure | Low-velocity near seafloor | Volcanic edifice |
| Pink and Orange sequences in Segment 2 | 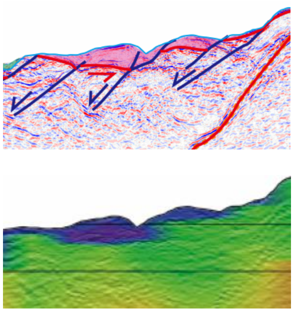 | Low amplitude, sub-horizontal reflectors beneath jagged seafloor | Low-velocity | Magmatic extrusive |
| Green sequence in Segments 2 and 3 | 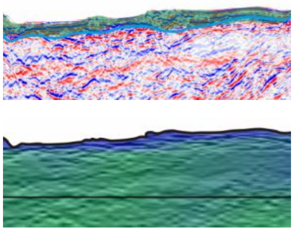 | Parallel, horizontal, and continuous reflectors beneath smooth seafloor | Low-velocity | Sediment |